Modeling of neutral hydrogen velocities in the Tokamak Fusion Test Reactor

D. P. Stotler, C. H. Skinner, R. V. Budny, A. T. Ramsey, D. N. Ruzic et al.

Related Articles

Effect of capacitive coupling in a miniature inductively coupled plasma source
J. Appl. Phys. 112, 093306 (2012)

Time dependent behaviors of ion-ion plasmas exposed to various voltage waveforms in the kilohertz to megahertz frequency range
Phys. Plasmas 19, 103501 (2012)

Electron scattering in helium for Monte Carlo simulations
Phys. Plasmas 19, 093511 (2012)

Generation of high-energy (>15 MeV) neutrons using short pulse high intensity lasers
Phys. Plasmas 19, 093106 (2012)

Improved modeling of relativistic collisions and collisional ionization in particle-in-cell codes
Phys. Plasmas 19, 083104 (2012)

Additional information on Phys. Plasmas

Journal Homepage: http://pop.aip.org/

Journal Information: http://pop.aip.org/about/about_the_journal

Top downloads: http://pop.aip.org/features/most_downloaded

Information for Authors: http://pop.aip.org/authors

Modeling of neutral hydrogen velocities in the Tokamak Fusion Test Reactor

D. P. Stotler,[a] C. H. Skinner, R. V. Budny, and A. T. Ramsey
Princeton Plasma Physics Laboratory, Princeton University, Princeton, New Jersey 08543

D. N. Ruzic and R. B. Turkot, Jr.
University of Illinois, 103 South Goodwin Avenue, Urbana, Illinois 61801

Monte Carlo neutral transport simulations of hydrogen velocities in the Tokamak Fusion Test Reactor (TFTR) [K. M. McGuire *et al.*, Phys. Plasmas **2**, 2176 (1995)] are compared with experiment using the Doppler-broadened Balmer-α spectral line profile. Good agreement is obtained under a range of conditions, validating the treatment of charge exchange, molecular dissociation, surface reflection, and sputtering in the neutral gas code DEGAS [D. Heifetz *et al.*, J. Comput. Phys. **46**, 309 (1982)]. A residual deficiency of 10–100 eV neutrals in most of the simulations indicates that further study of the energetics of H_2^+ dissociation for electron energies in excess of 100 eV is needed. © *1996 American Institute of Physics.* [S1070-664X(96)01411-5]

I. INTRODUCTION

Reliable predictions of parameters in the plasma boundary are crucial for the design of next-step devices such as the International Thermonuclear Experimental Reactor (ITER)[1] and advanced compact tokamaks such as the National Spherical Torus Experiment.[2] It is essential that the codes used for this task be benchmarked against experimental data. Spectroscopic data are ideal for this comparison since they are obtained without perturbations. In this paper, we use the DEGAS Monte Carlo neutral transport code[3,4] to simulate the spectrum of Balmer-α emissions as measured by a Fabry–Perot interferometer[5] in the Tokamak Fusion Test Reactor (TFTR).[6] The Doppler-shifted spectrum provides direct information about the velocity distribution of hydrogen atoms which determines the penetration of recycled hydrogen to the last-closed flux surface and the fuelling of the plasma core. Hence, the Balmer-α spectrum forms an ideal basis for benchmarking a kinetic code such as DEGAS.

This approach has been used for some time to investigate edge physics and validate models thereof.[7–15] The impact of detachment[9] and changes in edge temperature[10] on the Balmer-α spectra has been examined in the Tokamak Experiment for Technology Oriented Research (TEXTOR).[16,17] Later work by the same group[14] was focussed on benchmarking atomic and surface physics data in the Monte Carlo neutral transport code EIRENE[18] against the measured spectrum. Fielding *et al.*[11] compared spectra in gas puffing discharges on DITE with spectra from recycling. Modeling results predicted fewer low energy atoms than measured, leading them to suggest that the published atomic physics rate coefficients needed improvement.

This paper evaluates the applicability of atomic and surface physics data in the DEGAS code to the high temperature plasmas near the TFTR limiter. It builds upon previous work in which DEGAS has been used to simulate the spatial variation of Balmer-α emissions in TFTR,[19,20] and a wide variety of other devices, including Wendelstein 7-AS (W7-AS),[21]

GAMMA 10,[22] Alcator C-Mod,[23] DIII-D,[24,25] and PISCES-A.[26]

The Balmer-α line of hydrogen results from the radiative decay of the electron from the principal quantum state $n=3$ to $n=2$. The $n=3$ excited atoms typically arise from direct electron excitation of ground state neutral hydrogen atoms. The resulting photons are Doppler shifted according to the velocity of the atoms. Hence, the Balmer-α spectrum represents the velocity distribution of the emitting atoms.

Since the edge density is insufficient to thermalize the velocity distribution, the contributions of the various reaction pathways that generate hydrogen atoms may be associated with different wavelength regions (velocities) in the spectral profile. For example, atoms arising from the dissociation of H_2 molecules have an energy in the range 0.2–7.8 eV. Hydrogen atoms can also be sputtered from the surface material by incident ions and atoms of all species. These sputtered atoms have energies which are comparable to the surface binding energy; for the cases examined in this paper, the sputtered distribution peaks near 7 eV. Some atoms are the result of the reflection of ions off of the limiter and have energies

$$E_{\text{refl}} = R_E(E_i + \phi_{\text{sh}}), \tag{1}$$

where R_E is the fraction of the incident energy retained by the reflected atom (a function of the surface material and incident velocity), E_i is the ion energy, on the order of the local T_i, and ϕ_{sh} is the sheath potential, taken to be $3T_e$. Atoms resulting from charge exchange have a much higher energy, similar to that of the ion energy distribution in the plasma edge.

Alternatively, Balmer-α photons can arise *directly* from the dissociation of H_2 and H_2^+ into $H(n=3)$ product atoms. Because the energetics of these reactions are not the same as those of the more predominant processes which yield only ground state atoms, the resulting contributions to the spectrum are different from those due to ground state dissociation products.

The tritium capability of TFTR provides an opportunity to examine the physics of these processes with all three hydrogen isotopes. In this paper, the symbol ''H'' will be used mostly to refer to a generic hydrogen isotope; the occasions on which it refers to the lightest isotope will be clear from context.

In this paper, we compare the hydrogen velocity distribution predicted by the neutral transport code DEGAS to spectral measurements of the Doppler-broadened Balmer-α line profile. The paper is organized as follows. In Sec. II, the TFTR device and Fabry–Perot diagnostic are briefly described. The DEGAS code and the modifications made to it for the purpose of simulating the H_α spectrum are presented in Sec. III. In Sec. IV, the results of the simulations are described; sensitivity tests will be considered here as well. An alternative model for the dissociation of H_2^+ which can provide closer agreement with the experimental data is presented in Sec. V. Finally, our conclusions are given in Sec. VI.

II. MEASUREMENTS OF BALMER-α SPECTRUM IN TFTR

In this section we describe the experimental measurements of the Balmer-α line profile on TFTR. The TFTR plasma has a major radius that is typically between 245 and 262 cm and a circular cross section with minor radius in the range 80–90 cm. The plasma boundary is defined by an inner toroidal limiter composed of carbon composite tiles in the high heat flux regions and graphite tiles elsewhere, both supported by cooled inconel-718 backing plates.

Photons emitted from TFTR are collected by a telescope and transferred via a 1 mm fiber optic cable to a remote Fabry–Perot interferometer, which analyzes the spectrum.[5] The telescope views a region on the TFTR inner limiter 20 cm in diameter at the midplane. The Zeeman effect splits the H_α lines into an unshifted π component, polarized parallel to the field direction, and two σ components polarized perpendicular to the field. A polarizing filter is placed in front of the telescope lens and oriented to transmit only the unshifted π component. Fifty meters distant from the torus the light exits the fiber optic, is recollimated and input to an optical filter with 10 Å bandpass centered at 6561 Å, which transmits the H_α emission lines.

To resolve the individual spectral lines, the light emerging from the filter is refocused into a short optical fiber and input to a Fabry–Perot interferometer. The free spectral range of the Fabry–Perot is 7 Å, and its resolution is 0.23 Å. The Fabry–Perot repetitively scans over the wavelength region. An electronic controller maintains constant Fabry–Perot cavity separation and optimal alignment.

Since the line profile is scanned in time, the line shape is sensitive to time-dependent changes in the overall emission. A beam splitter intercepts a fraction of the light entering the Fabry–Perot and reflects it via another optical fiber to a second photomultiplier with a second 10 Å bandpass interference filter centered at the D_α wavelength. In this way the total $H_\alpha + D_\alpha + T_\alpha$ emission from the plasma region is recorded and can be used to normalize the line profile and remove the effects of fluctuations.
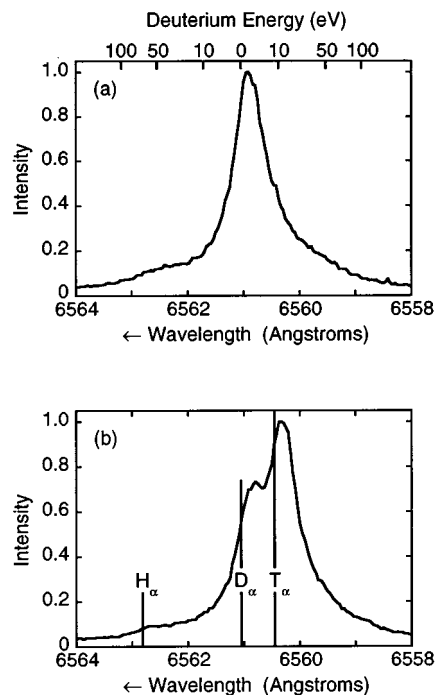

FIG. 1. Observed Balmer-α spectral profile (a) in a deuterium discharge, (b) in a discharge with strong tritium gas puffing. The energy scale included in (a) represents the equivalent energy of a deuterium atom at each wavelength. The line centers of the three isotopes are indicated in (b).

Figure 1 shows two experimental spectra, one with only hydrogen and deuterium, and one from a similar discharge with all three isotopes: hydrogen, deuterium and tritium. The rest wavelengths of H_α, D_α and T_α are 6562.80, 6561.04, and 6560.45 Å.

The relatively high tritium fraction in Fig. 1(b) is the result of strong tritium gas puffing into the discharge in a campaign to study the isotope scaling of low-confinement mode (L-mode) plasmas.[27] While the peaks are resolved, the line wings are blended. Since the densities are insufficient to thermalize the atomic velocity distribution, the profiles are not Gaussian. Wavelengths shorter than the rest wavelength (to the right of the line center in Fig. 1) correspond to atoms with velocities directed away from the inner limiter and into the plasma. Emissions on the long wavelength side originate from atoms moving toward the limiter; some atoms impinge on the limiter without being excited. This causes an erosion of the long wavelength wing relative to the short wavelength side.[28] Additionally, sputtered atoms contribute only to the short wavelength wing so that the line profile is asymmetric. As indicated by the energy scale in Fig. 1(a), neutral hydrogen atom energies are predominantly in the range 1–5 eV. The corresponding velocities, at 5 eV for example, are 3.1×10^6 cm/s for H, 2.2×10^6 cm/s for D, and 1.8×10^6 cm/s for T.

The tritium capability of TFTR has provided an important opportunity to compare the velocity distribution of tritium and deuterium. To first order, one expects the tritium velocity to be lower by a factor $(2/3)^{1/2}$ due to the mass difference. However, there are possibly other differences. During dissociation, the lower velocity of the tritium atoms
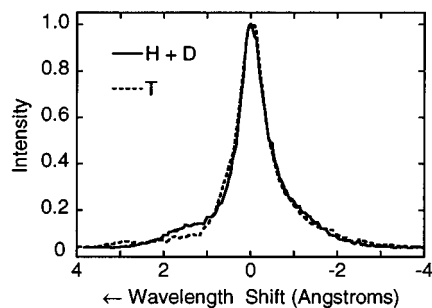
FIG. 2. Comparison of D_α and T_α spectral line shapes. The D_α line, labeled H + D, was taken prior to tritium beam injection and contains contributions from H. The T_α line shape is obtained by subtracting from a DT discharge the D_α contribution and rescaling the wavelength scale by the square-root of the T to D mass ratio.

FIG. 3. Typical TFTR mesh used by DEGAS. The chords used to compute the poloidal variation of the H_α emission are indicated. The poloidal extent of the limiter is depicted by the heavy line. The shaded region just above midplane represents the observation volume of the Fabry–Perot interferometer; the region used by DEGAS covers the hatched region as well.

can influence the pathways of molecular breakup. For example, Higo[29] found evidence for isotope effects originating from the different Frank–Condon region widths, nuclear masses, and curve crossing probabilities. In addition, since the tritium neutrals are moving more slowly than those of deuterium they will experience, on average, a different plasma environment.

In order to highlight variations in the line profiles beyond the mass scaling we have analyzed the line profiles of Fig. 1. The deuterium contribution in the #88484 profile [Fig. 1(b)] must be subtracted in order to uncover the tritium profile. To estimate the deuterium contribution we fit the composite line profile to six trial Gaussians, two for each isotope plus a first order background. The number of free parameters is reduced from 20 to 8 by using the known wavelength differences and the mass scaling factor. The fitting shows a composition of 8% H, 38% D and 54% T. Discharge #88638, with deuterium puffing, has the same plasma current, major radius, as well as similar rf heating power and electron density. We scale the deuterium spectral profile from discharge #88638 [Fig. 1(a)] to correspond to 38% of #88949 and subtract it, yielding a profile representing the T_α line alone. The wavelength scale of this profile is then multiplied by a factor $(3/2)^{1/2}$. Figure 2 shows this profile together with the deuterium profile from Fig. 1(a). Differences in the velocity distribution beyond the mass scaling factor should show up as differences between the spectral line shapes. It can be seen that the profiles are very similar. There is a trace of hydrogen present in one profile, otherwise isotopic differences beyond the $(3/2)^{1/2}$ factor are too small to resolve. In DEGAS, the mass scaling factor is used in calculating the velocities of the different hydrogen isotopes, all the other atomic data are taken to be independent of isotopic species.

III. DEGAS SIMULATIONS

DEGAS[3,4] is a three-dimensional Monte Carlo neutral gas transport code. The geometry and plasma conditions of the experiment are specified as input, then neutral atoms and molecules are followed in a Monte Carlo fashion as they undergo ionization, charge exchange, dissociation, and sur-
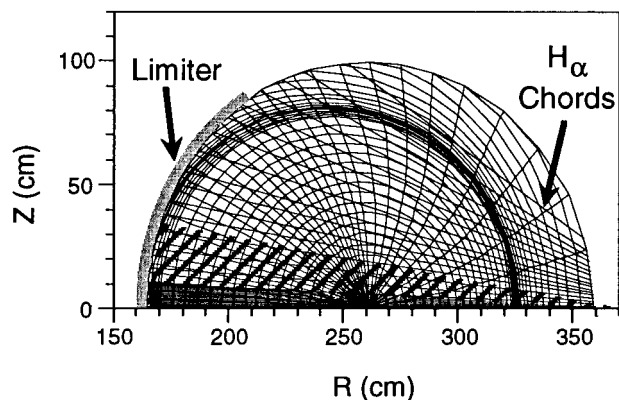
face interactions. The result is, in effect, a numerical solution of the Boltzmann equation for the neutral distribution function.

A. TFTR geometry and plasma parameters

In this work, toroidal symmetry is assumed. Hence, two-dimensional data are input and output, although neutral tracking is still done in three dimensions. Up–down symmetry is assumed; only the upper half of the plasma is simulated.

The computational mesh is based upon the magnetics data for the TFTR shot of interest. Namely, the TRANSP[30] plasma analysis code computes a two-dimensional magnetic equilibrium from these data; the flux surface shapes inside the last-closed flux surface (LCFS) are given in terms of moments of $\cos\theta$ and $\sin\theta$, where θ is a poloidal angle. A code which serves as a preprocessor to DEGAS obtains these moments from the TRANSP database and reconstructs the flux surface shapes. It then subdivides the surfaces in the poloidal direction at a set of convenient angles. Finally, this mesh is linearly extrapolated out to the material boundaries which are specified using detailed information about the limiter and vacuum vessel hardware. A typical geometry is shown in Fig. 3.

TRANSP models the time evolution of the plasma parameters using measurements as input. Typically these include time-dependent profiles of the electron density, electron and impurity (generally carbon) temperatures, and impurity toroidal velocity. The Z_{eff} is inferred from visible bremsstrahlung observations. When available, profiles of the safety factor or of the pitch angle can be provided as well. Within the LCFS, we take the plasma densities and temperatures directly from TRANSP. However, TRANSP does not simulate the scrape-off layer, and there are no density or temperature measurements available for this region. As is described in Ref. 20, an exponential fall-off is assumed for the plasma density and temperature outside of the LCFS; their length scales are taken to be the same, $\Lambda_n = \Lambda_T \equiv \Lambda$.

The flux of H^+ to the limiter is given by

$$\Gamma_{H^+} = \alpha n_{H^+} C_s \sin(\theta + \gamma), \qquad (2)$$

where n_{H^+} is the H^+ density, C_s is the sound speed (n_{H^+} and C_s are evaluated just in front of the limiter), and θ is the field line angle of incidence in the poloidal plane. The parameter γ is an additional ''filling factor'' incorporated to account for perpendicular transport effects which give rise to nonzero emissions observed[31] near midplane where $\theta \to 0$. The constant α is included to indicate that the total current to the limiter (summed over species) can be set arbitrarily since the neutral transport problem being solved is linear.

Experimental H_α measurements are made along five cords at various heights on the inner limiter. Chordal integrals of the DEGAS simulated emissions are computed along a more closely spaced set of chords (Fig. 3) and compared with these data. The two adjustable scrape-off layer parameters Λ and γ are varied to optimize the match between observed and simulated emissions. The value of the parameter α in Eq. (2) is derived from the measured absolute intensity of the H_α emissions.

B. Surface physics

The sputtering of hydrogen isotopes from the graphite limiter by incident carbon and hydrogen provides a significant particle source for TFTR plasmas with yields comparable to the expected particle reflection coefficients. Furthermore, these sputtered atoms have an energy distribution significantly different from those resulting from reflection or desorption.

To estimate the sputtering yields and reflection coefficients, the VFTRIM3D code is used. VFTRIM3D, based on the TRIM code,[32] utilizes a Monte Carlo model to simulate binary collisions within a solid. It tracks the cascade of atoms generated by an incident atom until they leave the surface (sputter or reflect) or lose enough energy that they cannot escape. VFTRIM3D[323] extends the TRIM concept to treat rough surfaces that are prescribed by a fractal model, with the fractal dimension varied to best match the roughness of the actual experimental surface.

Sputtering yields $Y_{i \to j}$ (the number of atoms of species j sputtered as a result of one incident atom of species i) and reflection coefficients R_i are generated for four species: H, D, T and C, incident at four energies: 100, 500, 1000 and 3000 eV, on graphite saturated with deuterium (4 atoms of deuterium for every 10 carbon atoms). An incident polar angle of 45 degrees is assumed for all cases, based on previous investigations by Hua and Brooks.[34]

The inclusion of carbon sputtering is critical since the yields due to incident carbon are much larger than those resulting from the hydrogen species. To simulate carbon directly in DEGAS would require density profiles and limiter fluxes for each carbon charge state, but these experimental data are not currently available. Instead, the carbon sputtering yield is combined with that of deuterium to form an effective yield

$$\Gamma_{D,sput} = \Gamma_{D,in} \left(Y_{D \to D} + \frac{\Gamma_{C,in}}{\Gamma_{D,in}} Y_{C \to D} \right), \qquad (3)$$
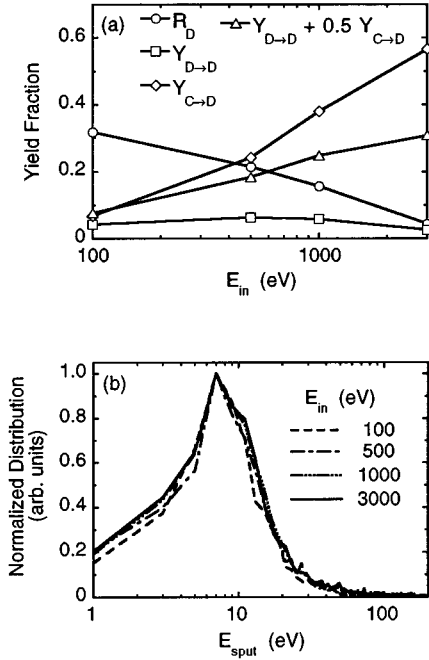

FIG. 4. Plot of (a) deuterium sputtering yields and reflection coefficients as a function of incident energy; (b) normalized sputtered deuterium energy distributions at four incident carbon energies. In (a), the separate deuterium sputtering contributions from incident deuterium and carbon are included along with the effective yield, Eq. (3), used in the code.

where Γ is the particle flux. The subscript ''in'' denotes incident; ''sput,'' sputtering. The ratio $\Gamma_{C,in}/\Gamma_{D,in}$ is treated as an adjustable parameter. Values of order unity are expected from Z_{eff} measurements. For the present work $\Gamma_{C,in}/\Gamma_{D,in} \simeq 0.5$ provides the best match with the experimental H_α spectrum.

Figure 4(a) shows the deuterium reflection coefficient and sputtering yields of deuterium as calculated by VFTRIM3D due to incident deuterium and carbon as a function of incident energy. The reflection probability falls with increasing energy; that is, it becomes more likely that the projectile energy will be transferred to the target (lattice) atoms. Sputtering occurs when these atoms absorb sufficient energy to reach and escape the surface.

A list of ~ 1000 random velocity vectors is generated from the VFTRIM3D flights for each process, incident energy, and species combination. These lists are read into DEGAS at the start of a simulation. When a reflection or sputtering occurs, the next vector is taken from the appropriate list and used to specify the particle velocity.

Figure 4(b) shows the energy distribution of sputtered deuterium resulting from incident carbon and deuterium. The distributions have been normalized to emphasize the relative insensitivity to the incident energy. Analytically, the energy distribution of sputtered atoms is often taken to be a Thompson distribution[35,36]

$$\frac{dY}{dE} \propto \frac{E}{(E + E_S)^3}, \qquad (4)$$

where E is the sputtered energy and E_S is the surface binding energy of the material. This distribution is explicitly independent of the incident energy.

The VFTRIM3D simulated distributions differ in general from those of Eq. (4). In these VFTRIM3D calculations, the binding energy for carbon is 7.4 eV; the peak of the Thompson energy distribution is at 3.7 eV. However, deuterium atoms heading out of the material lose energy to the lattice atoms inefficiently (compared with carbon) as a consequence of the scaling of the maximum binary collision transfer energy with mass (see, for example, Ref. 37):

$$\frac{\Delta E}{E_{\text{in}}} = \frac{4 m_p m_t}{(m_t + m_p)^2}, \tag{5}$$

where m_p and m_t are the projectile and target masses. Thus, deuterium atoms leave the surface with a higher energy [peaking at 7 eV in Fig. 4(b)] than one would expect based on Eq. (4).

The average sputtered energy increases[35,36] from 11 eV at $E_{\text{in,D}} = 100$ eV to 40 eV at $E_{\text{in,D}} = 3000$ eV as a result of contributions from tail atoms with energies much greater than the peak energy of 7 eV [Eq. (5) indicates that up to ~ 0.5 of an incident carbon's energy can be transferred to a sputtered deuterium atom]. Such atoms are too few in number and at too high an energy to be apparent in Fig. 4(b).

The average reflected energy $\bar{E}_{\text{refl,D}}$ of a deuterium atom rises linearly with incident energy $E_{\text{in,D}}$; for these VFTRIM3D runs

$$\bar{E}_{\text{refl,D}} \simeq 0.4 E_{\text{in,D}}. \tag{6}$$

This is again a consequence of Eq. (5).

We take advantage of Eq. (6) to map continuous values of E_{in} on to the four discrete incident energies in our model. The reflected velocity vectors from VFTRIM3D do a poor job of simulating low energy ($E_{\text{in,D}} \ll 100$ eV) reflections. In order to improve the DEGAS model, the energies associated with the random velocity vectors are rescaled according to

$$E_{\text{refl,}i} = E_{\text{in,}i} \left(\frac{E_{\text{refl,}i}^{k,l}}{E_{\text{in}}^l} \right), \tag{7}$$

where $E_{\text{in,}i}$ and $E_{\text{refl,}i}$ are the incident and reflected energies of species i, respectively; $E_{\text{refl,}i}^{k,l}$ is the kth entry in the list of species i outgoing reflected velocities at the lth discrete incident energy E_{in}^l which is closest to $E_{\text{in,}i}$.

C. Molecular physics

In this section we describe the model used by DEGAS to determine the products of molecular dissociation and their velocities.

Even in the high temperature edge region of TFTR, most of the recycling is in the form of molecules.[38] Namely, incident hydrogen atoms and ions which do not result in reflection or sputtering are adsorbed:

$$R_i + \sum_j Y_{i \to j} + f_a A_i + (1 - f_a) A_i \equiv 1, \tag{8}$$

where A_i is the fraction of incident isotope i which is adsorbed. Of these, f_a are permanently adsorbed; $1 - f_a$ are

TABLE I. Electron-molecule reactions in DEGAS; E_{diss} is the energy of the dissociation products.

Label	Reaction	Ref. 39 Designation	E_{diss} (eV)
A	$e + H_2 \to e + H(1s) + H(1s)$	(2.2.5)	3.0
B	$e + H_2 \to e + H(1s) + H^*(n=3)$	(2.2.8)	6.7
C	$e + H_2 \to 2e + H_2^+$	(2.2.9)	$\cdots$
D	$e + H_2 \to 2e + H(1s) + H^+$	(2.2.10)	7.8
E	$e + H_2^+ \to 2e + 2H^+$	(2.2.11)	0.4
F	$e + H_2^+ \to e + H(1s) + H^+$	(2.2.12)	4.3
G	$e + H_2^+ \to e + H^+ + H^*(n=3)$	(2.2.13)	1.5
H	$e + H_2^+ \to H(1s) + H^*(n=3)$	(2.2.14)	5.1

desorbed. For most of this work, the inventory of hydrogen species in the limiter is taken to be constant so that $f_a = 0$. Desorbed hydrogen isotopes are assumed to be released as room temperature molecules. The sum of the reflection coefficient and sputtering yields for incident hydrogen ions in the energy range of interest is ~ 0.4. This implies that under steady-state conditions the remaining 0.6 re-enter the plasma as molecules.

The isotopic mix of incident hydrogen ions is adjusted to match that experimentally observed in the Balmer-α spectral profile. In those cases where the incident hydrogen (ion or atom) leads to a desorbed molecule, the isotope of one atom in that molecule is the same as the incident one. The isotope of the second atom is sampled from the species distribution of the incident flux; this is consistent with a constant isotopic inventory assumption.

Molecular hydrogen entering the plasma is dissociated by electron collisions. The energy of the hydrogen product atoms depends on the particular dissociation pathway and the energy transferred from the electron. An extensive tabulation of reaction rates and product energies is given in Ref. 39. The eight most significant molecular reaction (Table I) are explicitly included in DEGAS using the reaction rates from Ref. 39 (the reaction rate for pathway G has been scaled from the data in Ref. 39 following the prescription of Ref. 14). The product energies are also taken from Ref. 39 with two exceptions.

For reaction B experimental measurements of the product energies have been reported.[29] The product energies have been found to depend on the incident electron energy and form a bimodal distribution with peaks around 0.25 and 6.7 eV. For $T_e < 13$ eV, DEGAS assigns the dissociation products an energy of 0.25 eV; for $T_e > 90$ eV, the products are equally divided between 0.25 eV and 6.7 eV. For $13 < T_e < 90$ eV, the fraction in each channel varies smoothly between these two limits.

In reaction H, Ref. 39 assumes that all of the incident electron's energy is absorbed by the intermediate excited H_2 molecule. This leads to surprisingly high product energies at the edge temperatures found in TFTR ($T_e \gtrsim 100$ eV). There are no experimental data or theoretical calculations indicating product energies of this magnitude. Instead, we follow an analysis[40] similar to that done for reaction F in Ref. 39 and set the product energy for reaction H to 5.1 eV. This point will be discussed further in Sec. V.

Stotler *et al.*

TABLE II. Simulated TFTR time-slices.

Case	Shot	Time (s)	D + T NB Power (MW)	R (cm)	Avg. H_α (s^{-1})	Comment
1	76770	3.5	0 + 0	252	1.6×10^{13}	Ohmic
2	76770	4.0	14 + 20	252	2.1×10^{14}	Supershot
3	86231	3.9	8 + 9	245	2.1×10^{14}	Supershot
4	75830	3.9	20 + 0	252	3.8×10^{14}	L-mode

While the photons resulting from reactions B and G are tabulated during the DEGAS simulations, the number of product atoms from these pathways is negligible compared to those from reactions A and F. To reduce the complexity of the calculation, the products of reactions B and G are not tracked.

Since the present version of DEGAS does not handle ion transport, the H_2^+ ions are dissociated in the code as soon as they are formed. This is a good approximation in the TFTR edge due to the short mean free path for H_2^+ dissociation.

D. Spectrum computation

The Balmer-α spectrum recorded by the Fabry–Perot interferometer is simulated in DEGAS by logging the wavelengths of H_α photons emitted within the observational volume of the detector. The input data describing the observational volume are its direction and angular width. To reduce the simulation time required to obtain a given statistical accuracy, the width of the observational volume used in the DEGAS is larger than the actual width (Fig. 3). Since the DEGAS simulations are toroidally symmetric, the toroidal extent of the detector is ignored.

The H_α emission wavelength is Doppler-shifted according to the velocity of the H atom along the line-of-sight to the detector:

$$\lambda = \lambda_{0,i}\left(1 + \frac{\vec{v}_i \cdot \vec{x}_{FP}}{c}\right), \quad (9)$$

where $\lambda_{0,i}$ is the wavelength of the line center for isotope i, $\vec{v}_i$ is the neutral velocity, and $\vec{x}_{FP}$ is its position vector relative to the detector. Bins are set up in wavelength space; scores at each wavelength are made according to the local photon emission rate and the neutral's Monte Carlo statistical weight.[3] Emissions are further classified according to the physical process which gave rise to the emitting atom, allowing us to identify the relative contribution of each process to the total spectrum.

The local rate of H_α emission by the ground state atoms tracked by DEGAS is

$$R_{H_\alpha} = \left[\frac{N_H^0(n=3)}{N_H^0(n=1)}\right] A_{32}. \quad (10)$$

The ratio of $n=3$ to ground state densities is the result of a collisional radiative calculation for hydrogen[41] and is a function of the electron density and temperature.

The photons emitted directly by molecular dissociation products (reaction pathways B, G, and H) are logged in an analogous way, except that the local photon emission rate is governed by the reaction rate of these pathways rather than Eq. (10).

IV. RESULTS

We will examine in detail the spectra from four time-slices of three TFTR discharges (Table II). Cases (2) and (3) are high performance ''supershot'' discharges[42] with low deuterium edge density (Fig. 5); these two differ principally in that case (2) has a larger major radius. Case (1) is a time-slice from the same discharge as case (2), but prior to neutral beam injection. The third discharge, case (4), is in the L-mode regime, characterized by high deuterium edge density. Case (4) has deuterium only neutral beam heating; cases (2) and (3) have both deuterium and tritium neutral beams.

While a well-resolved tritium peak is clearly evident in discharges with strong tritium gas puffing [as in Fig. 1(b)], this has not been the case in shots with tritium neutral beam injection. Our experience with tritium neutral beam injection is that the fraction of T_α is generally low. The maximum fraction of $T_\alpha/(H_\alpha + D_\alpha + T_\alpha)$ observed to date is 11%, after 8 discharges heated by tritium only neutral beam injection.[43]

The fraction of T_α in the spectrum is estimated from the difference in the normalized line profiles in the region of the T_α wavelength between the shot of interest and a similar
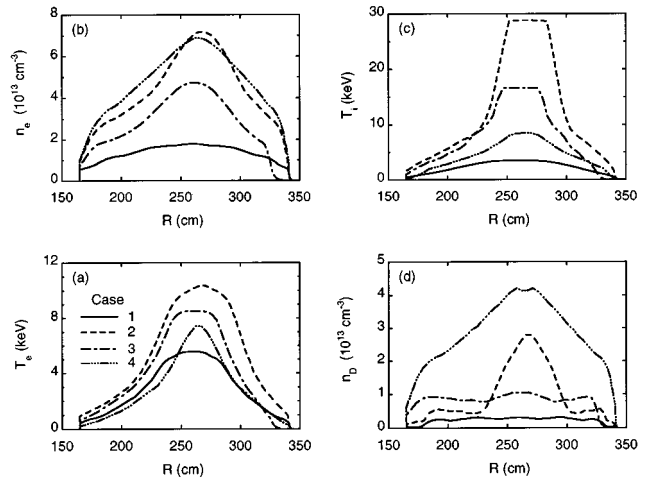

FIG. 5. Profiles of the (a) electron temperature, (b) electron density, (c) ion temperature, and (d) ion density as a function of major radius for the four cases described in Table II. The measured ion temperature profiles are typically very noisy near the axis; however, as is shown here, these variations are effectively smoothed by TRANSP. This has no impact on the H_α spectrum which originates well away from the axis.
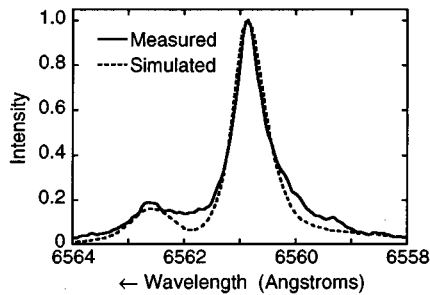
FIG. 6. Comparison of simulated and measured spectra for case (2). Note that the simulated spectrum has been convoluted with the experimental instrument function for this comparison.
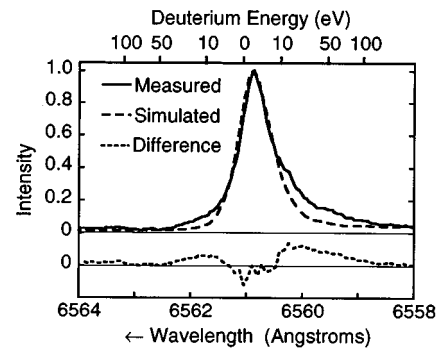

FIG. 7. Measured and simulated spectra for case (3) with hydrogenic contributions removed; the difference of the two spectra is shown on the lower scale. The energy scale in the figure is computed for deuterium relative to line center.

discharge performed prior to tritium injection.[5] The absence of tritium in the comparison discharge is independently confirmed by a low DT neutron signal. For the TFTR discharges simulated in this paper, more than 75% of the hydrogen isotope recycling is deuterium. Hydrogen (i.e., protium), an intrinsic impurity in the limiter tiles, accounts for $\leqslant 20\%$ and tritium $<4\%$. The limiter fluxes used in DEGAS are initially taken to have these same proportions; the H fraction is refined if necessary to improve the match to the measured spectrum.

A comparison of the measured and simulated spectra for case (2) (Fig. 6) shows good agreement. The width of the main D_α peak is reproduced well by the simulation, as is the tail at the highest energies shown. The former indicates that, first, there is a substantial source of desorbed hydrogen molecules (as opposed to desorbed hydrogen atoms) and, second, that the energies of the dissociation products used by DEGAS are essentially correct. Sputtering also provides a significant contribution to the width of the main peak. Agreement at the highest energies demonstrates that charge exchange and reflection are being adequately simulated.

A discrepancy between the measured and simulated spectra is apparent on both sides of the D_α line center. The inadequacies in the DEGAS deuterium physics leading to the discrepancy on the short wavelength side of the D_α peak are likely manifested again for H on the short wavelength side of the H_α line center. The low simulated signal between the H_α and D_α also results from the absence of sputtered H in the model (in the VFTRIM3D sputtering calculations, the surface is assumed to be saturated with *deuterium only*).

However, in Fig. 7 we demonstrate using case (3) that the deficiencies in the D_α spectrum on the long wavelength side are not due to H alone. The H_α contribution has been removed from the interferometer data by rescaling the deuterium peak for a similar discharge to account for the H / D mass ratio [spectral width $\propto (\text{mass})^{1/2}$] and the hydrogen concentration, and then subtracting from the case (3) spectrum. In the simulations, this effect is accomplished simply by disabling emission from H atoms. The difference of the resulting simulated and measured spectra is shown on the lower scale of Fig. 7.

Most of this difference is symmetric about the line center with energies in the 10–100 eV range. This symmetry

suggests that the missing atoms are the product of molecular dissociation. Unfortunately, there appear to be few experimental studies of the energies of dissociation products at the electron energies of interest (~ 100–1000 eV); we will return to this point in Sec. V.

The energy range of the discrepancy argues against other processes being responsible. First, charge exchange can be ruled out given that the local plasma temperatures are expected to be at least several hundred eV. And, as is indicated in Fig. 4, the sputtered energy distribution peaks at 7 eV, too small to explain this discrepancy. Even if the sputtered energy distribution were considerably wider than that computed by VFTRIM3D, there would still be a deficiency on the long wavelength side of the D_α peak.

The measured spectra from cases (1) and (4) are very similar to those of (2) and (3) [Fig. 8(a)]. Apart from the
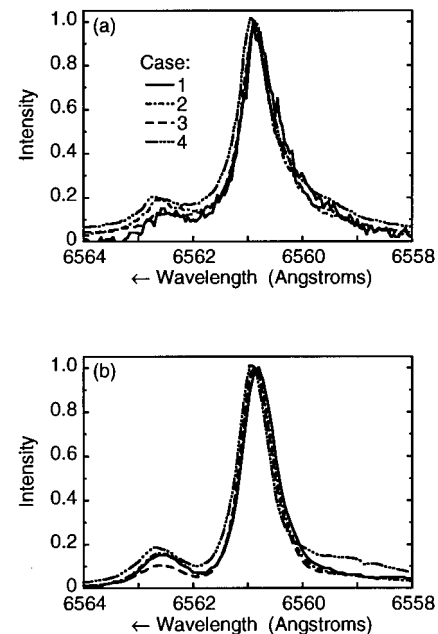

FIG. 8. Measured (a) and simulated (b) spectra from the four cases described in the text.

FIG. 10. Comparison with experiment of case (2) and a simulation made with the prior version of DEGAS which did not have deuterium sputtering.
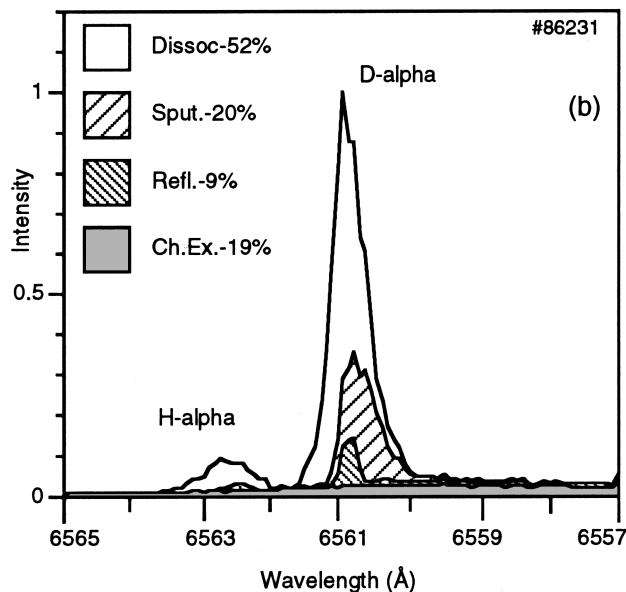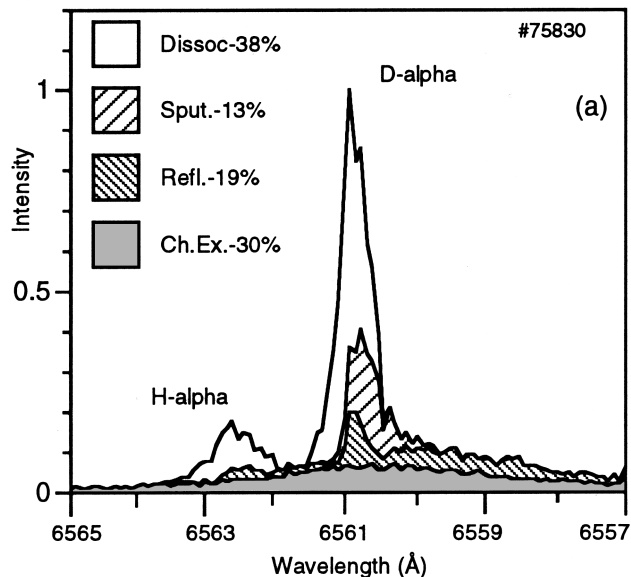
FIG. 9. The simulated spectra for cases (4) [in part (a)] and (3) [part (b)] are broken down into the contributions made by each physical process. The relative areas of these contributions are reported in the legend. These spectra have not been convoluted with the experimental instrument function unlike the other simulated spectra presented in this paper. The lack of a sputtered component in the H spectral profile is a computational limitation.

charge exchange atoms which are more compatible with the wavelength scale in Fig. 9 (energies < 150 eV); the corresponding atoms in supershots will have energies in the keV range and are off-scale in Fig. 9.

We now examine the sensitivity of the spectrum to other factors.

A. Sputtering

Sputtered atoms make a significant contribution to the H_α spectrum in TFTR (Fig. 9). The importance of sputtering in achieving a good match against the measured spectrum is made clearer in Fig. 10 where we show the spectral profile obtained with the previous version of DEGAS which did not include sputtering. In this case, the fraction of atoms that would have been sputtered instead enter the plasma as molecules, yielding lower energy contributions to the spectrum (Fig. 9). Hence, without sputtering the spectrum is even narrower in precisely the energy range where the simulation is already producing too few atoms.

Chemical sputtering, another potential source of neutral hydrogen, is not believed to be important in these TFTR discharges. The principle reason is that none of the molecular bands associated with methane have been observed with a multichannel visible spectrometer. Second, chemical sputtering is expected to be important only at wall temperatures higher than those[38,44] typical of the TFTR limiter.

B. Lithium coatings

The injection of lithium pellets[45,46] into TFTR discharges can dramatically reduce the edge carbon and hydrogen densities, leading to enhanced supershot performance. Recent investigations point to hydrogen pumping by the lithium as a contributor to lower edge density.[47,48]

However, the measured H_α spectra in TFTR discharges with and without lithium injection do not differ significantly. In this subsection, we use this insensitivity to place bounds on the lithium content of the limiter surface.

We examine the energy distribution of sputtered deuterium predicted by VFTRIM3D for deuterium-saturated, lithium-impregnated, graphite surfaces. As in Sec. III B, atoms of deuterium and carbon are assumed to impinge upon a deuterium-saturated graphite surface at 500 eV and 45 degrees. Six runs are made in which the lithium concentration in the top 50 Å is taken to be 0, 5, 10, 25, 50, and 100%.

variation in H concentration, the only discernible difference is that the wings of the L-mode spectrum [case (4)] are broader. An overlay of the corresponding simulated spectra yields the same behavior [Fig. 8(b)].

The broader wings of the L-mode case [Fig. 9(a)] appear to be due to larger contributions from charge exchange and reflection than in the supershot discharge, case (3) [Fig. 9(b)]. The former is partially the result of the higher n_D/n_e near the limiter in L-mode (see Fig. 5) relative to supershots. The latter is associated with the higher reflection coefficients (Fig. 4) in effect at the low L-mode edge temperatures. The lower temperatures also lead to energies for reflected and
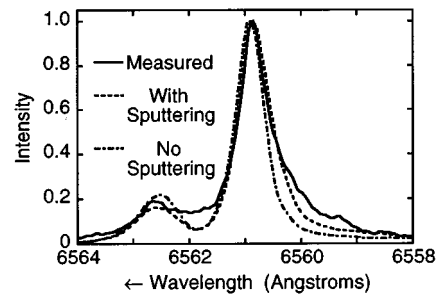
Phys. Plasmas, Vol. 3, No. 11, November 1996
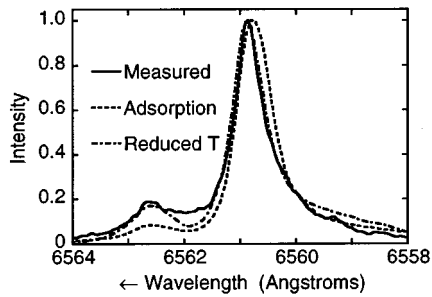
Stotler et al. 4091

FIG. 11. Comparison with experiment in case (2) of two simulations, one featuring 80% adsorption and the other reduced edge temperature values.

Since sputtered atoms arise from within the top few angstroms of the surface, these results should not be sensitive to the depth of the lithium-containing region.

Of crucial importance to the energy distribution predicted by VFTRIM3D, and consequently to the simulated H_α spectrum, is the binding energy used for the surface. At 1.7 eV, the surface binding energy of lithium is much smaller than the 7.4 eV used for graphite.[37] Following Ref. 45, we take the binding energy of the composite surface to be a weighted average of these two values. Thus, as the fraction of lithium is increased the peak of the sputtered deuterium energy spectrum falls to lower energies, reaching 2 eV at the 100% lithium limit.

The observed insensitivity of the experimental spectrum to the addition of lithium indicates that the neutral energy distribution changes in the process by less than a few eV, the energy uncertainty of the measurements. If the sputtered contribution to the experimental spectrum is indeed significant, as is suggested by Fig. 9, we estimate that a drop in the peak of the sputtered energy distribution from 7 eV to less than 5 eV would be noticeable. This would place an upper bound on the lithium concentration at 50% according to the VFTRIM3D simulations.

C. Net adsorption

A better match on the short wavelength side of the D_α line could be obtained by enhancing the *relative* contribution of sputtered deuterium. This could be achieved by reducing the contributions made by molecular dissociation products. As was described in Sec. III C, the dissociation contribution is determined by the constraint of no net adsorption. If there were net adsorption, there would be fewer hydrogen molecules entering the plasma per incident ion.

Analysis of the experimental data, however, argues that the limiter acts as particle source rather than a sink. In TFTR supershots, there is no gas feed during the discharge, while in the L-mode case (4), there is a helium puff at 3.6 s.

As is shown in Fig. 11, adsorbing 80% of all hydrogen atoms and molecules striking the limiter in case (2) leads to a somewhat better match to the short wavelength side of the D_α line center, but not to the long wavelength side. Note that the absence of sputtering of H in the model is responsible for the large discrepancy near the H_α line center. Although the addition of sputtering of H would improve the agreement on the long wavelength side of D_α, it would seem unlikely to eliminate it. We conclude that net adsorption cannot resolve the discrepancy between simulation and experiment.

D. Variations in edge and scrape-off layer parameters

Variations in the plasma scrape-off layer scale length Λ which preserve the simulation's agreement with the poloidal H_α profile do not give rise to noticeable changes in the predicted H_α spectrum. Near midplane, the distance between the LCFS and the limiter is very short. The lack of sensitivity of the spectrum is thus expected because of the relatively small volume of the scrape-off layer being viewed by the interferometer. Even variations in the scrape-off length of a factor of two, sufficient to cause a clear discrepancy with the experimental poloidal H_α profile, do not result in significant modifications to the simulated spectrum.

On the other hand, we do expect sensitivity to the plasma parameters inside the LCFS. Note that the experimental error bars on the ion temperature, for example, are $\pm 5\%$ in the plasma edge region. However, as a hypothetical illustration, we repeat case (2) with electron and ion temperatures at the LCFS reduced to 100 eV (originally, $\simeq 900$ and 1500 eV, respectively). The temperatures are assumed to rise linearly up to the TRANSP-prescribed value at $r/a = 0.8$. The scrape-off layer scale length Λ used in case (2) is retained.

The resulting simulation yields a much improved match with the experimental measurements on the short wavelength side of the D_α line [Fig. 11(b)]. The reduced edge temperatures result in lower incident ion energies at the surface. As expected from Fig. 4, the fraction of reflected atoms increases while the number sputtered drops. Furthermore, the energies of the reflected atoms are reduced. They now make a substantial contribution in the energy range of the deficiency; previously they were thinly spread (Fig. 9) over a larger range. However, the deficiency on the long wavelength side of the D_α peak persists, suggesting that some other mechanism is responsible for the discrepancy. Also, as previously noted, such low LCFS temperatures are inconsistent with the experimental measurements.

Other physical effects which have been examined and found to have negligible impacts on the simulated spectrum are: Stark broadening, thermalization of H_2^+ on the background plasma, ion impact ionization and excitation of H, and reactions (3.2.6), (4.2.1), (4.3.1), (4.3.2), (4.3.3) of Ref. 39.

V. H_2^+ DISSOCIATION REVISITED

Given that the evidence points toward an explanation of the spectrum deficiency in terms of molecular dissociation products, we re-examine the present model for dissociation and consider possible alternatives. For electron temperatures in excess of 10 eV (certainly the case here), the $e + H_2$ reaction in Table I with the largest reaction rate (by a factor of ~ 8 for $T_e > 50$) is reaction C, ionization.[39] Since the electron cannot impart significant energy to the resulting ion in this reaction, we must turn our attention instead to the reactions involving H_2^+ in Table I, reactions F–H.

Higher energy H_2^+ dissociation products are plausible. Electron impact ionization of H_2 molecules populates vibrational levels in the ground state $X^2\Sigma_g^+ 1s\sigma_g\ H_2^+$. These H_2^+ molecules can be excited by electron impact in Frank–Condon transitions to high-lying repulsive molecular states (at the same internuclear separation) which then dissociate. H_2^+ formed from a H_2 molecule in the ground vibrational state is expected to have a distribution of vibrational states peaked around $v = 3$.[39] However, the vibrational distribution of H_2 molecules in TFTR is not known. Vibrationally excited H_2 would, when ionized, lead to an average $v > 3$ for H_2^+. At their inner turning points, these states provide access to high energy intermediate excited states which in principle could result in the absorption of > 20 eV of electron energy and, consequently, in higher energy dissociation products than are indicated in Table I.

With TFTR edge electron temperatures in the 100–1000 eV range, full absorption of the electron energy, such as was indicated in Ref. 39 for reaction H, would lead to dissociation products having energies *larger* than are needed to explain the spectrum deficiency. While there are published data on the cross sections of reactions F–H at these temperatures,[39,49,50] there are no data on the product energies. We believe that the actual product energies for these reactions lie between those in Table I and those obtained with full absorption of the electron energy. The present deficiency in the modeling of the 10–100 eV range underscores the need for excitation rate calculations in which the product energy is explicitly listed.

Changes in the reaction rates of these processes with vibrational distribution[51] should be accounted for in any revised model. If the result is a substantial reduction in the rate of the dominant reaction, reaction F, other processes such as proton impact dissociation may need to be added. However, the product energies of these pathways must also properly account for the vibrational state of the molecule.

VI. CONCLUSIONS

We have benchmarked the DEGAS neutral transport code against neutral deuterium velocities experimentally observed in TFTR. In the process, improvements have been made to the molecular hydrogen dissociation energies in the code and an explicit treatment of sputtered deuterium species has been added. Reasonable agreement between the measured and simulated spectra has been obtained under a variety of circumstances, validating the treatment of charge exchange, molecular dissociation, surface reflection, and sputtering in the code. However, a residual deficiency of neutrals in the 10–100 eV range has been noted. The fact that the missing portion of the spectrum is symmetric with respect to the D_α line center suggests that the explanation lies with molecular dissociation reactions. These results indicate the need for further investigation of the product energies of such reactions for $T_e \sim$ 100–1000 eV.

Recently, discharges with a high tritium density in the edge plasma have been generated in TFTR. These experiments have afforded a unique opportunity to measure the neutral tritium velocity distribution and to assess the validity of the standard extrapolation from measured deuterium velocities. Although there are several factors that could potentially lead to systematic differences in the deuterium and tritium velocities, the experimental measurements confirmed that the difference could be accounted for by the mass factor of $(3/2)^{1/2}$ (Fig. 2).

[1] G. Janeschitz, K. Borass, G. Federici, Y. Igitkhanov, A. Kukushkin, H. D. Pacher, G. W. Pacher, and M. Sugihara, J. Nucl. Mater. **220−222**, 73 (1995).

[2] S. M. Kaye (private communication, 1996).

[3] D. Heifetz, D. Post, M. Petravic, J. Weisheit, and G. Bateman, J. Comput. Phys. **46**, 309 (1982).

[4] D. B. Heifetz, in *Physics of Plasma-Wall Interactions in Controlled Fusion*, edited by D. E. Post and R. Behrisch (Plenum, New York, 1986), p. 728.

[5] C. H. Skinner, H. Adler, R. V. Budny, J. H. Kamperschroer, L. C. Johnson, A. T. Ramsey, and D. P. Stotler, Nucl. Fusion **35**, 143 (1995).

[6] K. M. McGuire, H. Adler, P. Alling, C. Ancher, H. Anderson, J. L. Anderson, J. W. Anderson, V. Arunasalam, G. Ascione, D. Ashcroft, C. W. Barnes, G. Barnes, S. Batha, G. Bateman, M. Beer, M. G. Bell, R. Bell, M. Bitter, W. Blanchard, N. L. Bretz, C. Brunkhorst, R. Budny, C. E. Bush, R. Camp, M. Caorlin, H. Carnevale, S. Cauffman, Z. Chang, C. S. Chang, C. Z. Cheng, J. Chrzanowski, J. Collins, G. Coward, M. Cropper, D. S. Darrow, R. Daugert, J. DeLooper, R. Dendy, W. Dorland, L. Dudek, H. Duong, R. Durst, P. C. Efthimion, D. Ernst, H. Evenson, N. Fisch, R. Fisher, R. J. Fonck, E. Fredd, E. Fredrickson, N. Fromm, G. Y. Fu, T. Fujita, H. P. Furth, V. Garzotto, C. Gentile, J. Gilbert, J. Gioia, N. Gorelenkov, B. Grek, L. R. Grisham, G. Hammett, G. R. Hanson, R. J. Hawryluk, W. Heidbrink, H. W. Hermann, K. W. Hill, J. Hosea, H. Hsuan, M. Hughes, R. Hulse, A. Janos, D. L. Jassby, F. C. Jobes, D. W. Johnson, L. C. Johnson, M. Kalish, J. Kamperschroer, J. Kesner, H. Kugel, G. Labik, N.T. Lam, P. H. LaMarche, E. Lawson, B. LeBlanc, J. Levine, F. M. Levinton, D. Loesser, D. Long, M. J. Loughlin, J. Machuzak, R. Majeski, D. K. Mansfield, E. S. Marmar, R. Marsala, A. Martin, G. Martin, E. Mazzucato, M. Mauel, M. P. McCarthy, J. McChesney, B. McCormack, D. C. McCune, G. McKee, D. M. Meade, S. S. Medley, D. R. Mikkelsen, S. V. Mirnov, D. Mueller, M. Murakami, J. A. Murphy, A. Nagy, G. A. Navratil, R. Nazikian, R. Newman, N. Norris, T. O'Connor, M. Oldaker, J. Ongena, M. Osakabe, D. K. Owens, H. Park, W. Park, P. Parks, S. F. Paul, G. Pearson, E. Perry, R. Persing, M. Petrov, C. K. Phillips, M. Phillips, S. Pitcher, R. Pysher, A. L. Qualls, S. Raftopoulos, S. Ramakrishnan, A. Ramsey, D. A. Rasmusen, M. H. Redi, G. Renda, G. Rewoldt, D. Roberts, J. Rogers, R. Rossmassler, A. L. Roquemore, E. Ruskov, S. A. Sabbagh, M. Sasao, G. Schilling, J. Schivell, G. L. Schmidt, R. Scillia, S. D. Scott, I. Semenov, T. Senko, S. Sesnic, R. Sissingh, C. H. Skinner, J. Snipes, J. Stencel, J . Stevens, T. Stevenson, B. C. Stratton, J. D. Strachan, W. Stodiek, J. Swanson, E. Synakowski, H. Takahashi, W. Tang, G. Taylor, J. Terry, M. E. Thompson, W. Tighe, J. R. Timberlake, K. Tobita, H. H. Towner, M. Tuszewski, A. von Halle, C. Vannoy, M. Viola, S. von Goeler, D. Voorhees, R. T. Walters, R. Wester, R. White, R. Wieland, J. B. Wilgen, M. Williams, J. R. Wilson, S. Yoshikawa, K. M. Young, M. C. Zarnstorff, V. Zavereev, and S. J. Zweben, Phys. Plasmas **2**, 2176 (1995).

[7] S. V. Mirnov and I. B. Semenov, At. Energy **28**, 129 (1970).

[8] P. Platz and TFR Group, J. Nucl. Mater. **93 & 94**, 173 (1980).

[9] U. Samm, H. L. Bay, P. Bogen, H. Hartwig, E. Hintz, K. Höthker, Y. T. Lie, A. Pospieszczyk, G. G. Ross, D. Rusbüldt, and B. Schweer, Plasma Phys. Controlled Fusion **29**, 1321 (1987).

[10] U. Samm, P. Bogen, H. Hartwig, E. Hintz, K. Höthker, Y. T. Lie, A. Pospieszczyk, D. Rusbüldt, B. Schweer, and Y. J. Yu, J. Nucl. Mater. **162−164**, 24 (1989).

[11] S. J. Fielding, P. C. Johnson, M. J. Forrest, D. Guilhem, and G. F. Matthews, J. Nucl. Mater. **162−164**, 482 (1989).

[12] D. H. McNeill, J. Nucl. Mater. **162−164**, 476 (1989).

[13] J. T. Hogan, C. C. Klepper, D. L. Hillis, and T. Uckan, J. Nucl. Mater. **162−164**, 469 (1989).

[14] D. Reiter, P. Bogen, and U. Samm, J. Nucl. Mater. **196−198**, 1059 (1992).

[15] S. Sekine, Y. Hirano, Y. Yagi, T. Shimada, Y. Maejima, H. Shimizu, and T. Tanabe, J. Nucl. Mater. **220−222**, 1135 (1995).

[16] H. Soltwisch, H. L. Bay, G. Bertschinger, P. Bogen, H. Conrads, K. H. Dippel, G. Fuchs, H. Gerhauser, B. Giesen, E. Graffman, E. Hintz, F. Hoenen, A. Kaleck, L. Könen, M. Korten, M. Lochter, N. Noda, A. Pospieszczyk, U. Samm, J. Schlüter, B. Schweer, F. Waelbroeck, G. Waidmann, L. H. Wei, P. Wienhold, J. Winter, and G. Wolf, Plasma Phys. Controlled Fusion **26**, 23 (1984).

[17] U. Samm, P. Bogen, H. A. Claassen, H. Gerhauser, H. Hartwig, E. Hintz, Y. T. Lie, A. Pospieszczyk, D. Rusbüldt, and B. Schweer, J. Nucl. Mater. **176 & 177**, 273 (1990).

[18] D. Reiter, in *Atomic and Plasma-Material Interaction Processes in Controlled Thermonuclear Fusion*, edited by R. K. Janev and H. W. Drawin (Elsevier, Amsterdam, 1993), p. 243, and references therein.

[19] D. H. Heifetz, A. B. Ehrhardt, A. T. Ramsey, H. F. Dylla, R. Budny, D. McNeill, S. Medley, and M. Ulrickson, J. Vac. Sci. Technol. A **6**, 2564 (1988).

[20] R. V. Budny and the TFTR Group, J. Nucl. Mater. **176 & 177**, 427 (1990).

[21] F. Sardei, P. Grigull, G. Herre, D. Hildebrandt, P. Pech, U. Wenzel, H. Wolff, and W7-AS Team, J. Nucl. Mater. **196−198**, 443 (1992).

[22] Y. Nakashima, K. Yatsu, K. Tsuchiya, M. Ichimura, N. Yamaguchi, M. Inutake, M. Shoji, K. Ohtoshi, T. Tamano, and S. Miyoshi, J. Nucl. Mater. **196−198**, 493 (1992).

[23] D. P. Stotler, J. A. Snipes, G. M. McCracken, B. LaBombard, M. Petravic, R. Vesey, S. Barle, G. Bateman, C. F. F. Karney, B. Lipschultz, J. L. Terry, and S. M. Wolfe, in *Plasma Physics and Controlled Nuclear Fusion Research, 1994*, Seville (International Atomic Energy Agency, Vienna, 1996), Vol. 3, p. 363.

[24] L. W. Owen, R. Maingi, D. K. Lee, P. K. Mioduszewski, D. R. Baker, D. L. Hillis, J. T. Hogan, G. L. Jackson, and M. R. Wade, J. Nucl. Mater. **220−222**, 315 (1995).

[25] M. E. Fenstermacher, G. D. Porter, M. E. Rensink, T. D. Rognlien, S. L. Allen, D. N. Hill, C. J. Lasnier, T. Leonard, and T. Petrie, J. Nucl. Mater. **220−222**, 330 (1995).

[26] A. Grossman, L. Schmitz, B. Merriman, R. Lehmer, F. Najmabadi, and D. P. Stotler, J. Nucl. Mater. **220−222**, 274 (1995).

[27] C. W. Barnes, S. D. Scott, M. G. Bell, R. Bell, R. V. Budny, C. E. Bush, E. D. Fredrickson, B. Grek, K. W. Hill, A. Janos, J. H. Kamperschroer, P. H. LaMarche, D. K. Mansfield, H. K. Park, C. K. Phillips, A. T. Ramsey, J. Schivell, B. C. Stratton, E. J. Synakowski, G. Taylor, J. R. Wilson, M. C. Zarnstorff, ''Confinement analysis in L-Mode of hydrogen isotope experiments on TFTR,'' submitted to Phys. Plasmas.

[28] A. Pospieszczyk, in Ref. 18, p. 213.

[29] M. Higo, S. Kamata, and T. Ogawa, Chem. Phys. **73**, 99 (1982).

[30] R. V. Budny, M. G. Bell, A. C. Janos, D. L. Jassby, L. C. Johnson, D. K. Mansfield, D. C. McCune, M. H. Redi, J. F. Schivell, G. Taylor, T. B. Terpstra, M. C. Zarnstorff, and S. J. Zweben, Nucl. Fusion **35**, 1497 (1995), and references therein.

[31] C. S. Pitcher, P. C. Stangeby, M. G. Bell, J. D. Elder, S. J. Kilpatrick, D. M. Manos, S. S. Medley, D. K. Owens, A. T. Ramsey, and M. Ulrickson, J. Nucl. Mater. **196−198**, 241 (1992).

[32] J. P. Biersack and L. G. Haggmark, Nucl. Instrum. Methods **174**, 257 (1980).

[33] D. N. Ruzic, Nucl. Instrum. Methods B **47**, 118 (1990).

[34] T. Q. Hua and J. N. Brooks, Phys. Plasmas **1**, 3607 (1994).

[35] J. Roth, in Ref. 4, p. 351.

[36] J. Roth, in Ref. 18, p. 381.

[37] W. Eckstein, *Computer Simulation of Ion-Solid Interactions* (Springer-Verlag, Berlin, 1991).

[38] J. Winter, J. Vac. Sci. Technol. A **5**, 2286 (1987).

[39] R. K. Janev, W. D. Langer, K. Evans, Jr., and D. E. Post, Jr., *Elementary Processes in Hydrogen-Helium Plasmas* (Springer-Verlag, Berlin, 1987).

[40] R. K. Janev (private communication, 1993). More generally, the expression for the product energy is $E_{\text{diss}} = 0.5(8.6 - 13.6/n^2)$ eV, where n is the principal quantum number of the excited product.

[41] J. Weisheit, J. Phys. B **8**, 2556 (1975).

[42] J. D. Strachan, Phys. Rev. Lett. **58**, 1004 (1987).

[43] P. C. Efthimion, L. C. Johnson, C. H. Skinner, J. Strachan, E. Synakowski, M. Zarnstorff, H. Adler, C. Barnes, R. V. Budny, J. Kamperschroer, W. W. Lee, M. Loughlin, D. McCune, A. T. Ramsey, G. Rewoldt, A. L. Roquemore, D. P. Stotler, W. M. Tang, and the TFTR Group, in Ref. 23, Vol. 1, p. 289.

[44] J. Roth, in Ref. 35, p. 389.

[45] J. A. Snipes, E. S. Marmar, J. L. Terry, M. G. Bell, R. V. Budny, R. J. Hawryluk, K. W. Hill, D. L. Jassby, D. K. Mansfield, D. M. Meade, H. K. Park, J. D. Strachan, B. C. Stratton, E. J. Synakowski, G. Taylor and the TFTR Group, D. N. Ruzic, and M. Shaheen, J. Nucl. Mater. **196−198**, 686 (1992).

[46] D. K. Mansfield, J. D. Strachan, M. G. Bell, S. D. Scott, R. Budny, E. S. Marmar, J. A. Snipes, J. L. Terry, S. Batha, R. E. Bell, M. Bitter, C. E. Bush, Z. Chang, D. S. Darrow, D. Ernst, E. Fredrickson, B. Grek, H. W. Herrmann, K. W. Hill, A. Janos, D. L. Jassby, F. C. Jobes, D. K. Owens, H. Park, A. T. Ramsey, A. L. Roquemore, C. H. Skinner, T. Stevenson, B. C. Stratton, E. Synakowski, G. Taylor, A. von Halle, S. von Goeler, K. L. Wong, and S. J. Zweben, Phys. Plasmas **2**, 4252 (1995).

[47] H. Sugai, H. Toyoda, K. Nakamura, K. Furuta, M. Ohori, K. Toi, S. Hirokura, and K. Sato, J. Nucl. Mater. **220−222**, 254 (1995).

[48] B. Terreault, H. Y. Guo, D. Kéroack, R. W. Paynter, W. W. Zuzak, G. Abel, M. Ennaceur, J.-L. Gauvreau, E. Haddad, L. Leblanc, G. G. Ross, H. H. Mai, N. Richard, B. L. Stansfield, TdeV Team, M. Caorlin, D. K. Owens, D. Mueller, S. Pitcher, P. H. LaMarche, J. D. Strachan, J. H. Arps, and R. A. Weller, J. Nucl. Mater. **220−222**, 1130 (1995).

[49] G. H. Dunn and B. Van Zyl, Phys. Rev. **154**, 154 (1967).

[50] J. M. Peek, Phys. Rev. A **10**, 539 (1974).

[51] M. A. Cacciatore, M. Capitelli, and R. Celiberto, At. Plasma Mater. Int. Data Fusion **2**, 65 (1992).